Inversion of multiwavelength Raman lidar data for retrieval of bimodal aerosol size distribution

Igor Veselovskii, Alexei Kolgotin, Vadim Griaznov, Detlef Müller,
Kathleen Franke, and David N. Whiteman

We report on the feasibility of deriving microphysical parameters of bimodal particle size distributions from Mie–Raman lidar based on a triple Nd:YAG laser. Such an instrument provides backscatter coefficients at 355, 532, and 1064 nm and extinction coefficients at 355 and 532 nm. The inversion method employed is Tikhonov's inversion with regularization. Special attention has been paid to extend the particle size range for which this inversion scheme works to ~10 μm, which makes this algorithm applicable to large particles, e.g., investigations concerning the hygroscopic growth of aerosols. Simulations showed that surface area, volume concentration, and effective radius are derived to an accuracy of ~50% for a variety of bimodal particle size distributions. For particle size distributions with an effective radius of <1 μm the real part of the complex refractive index was retrieved to an accuracy of ±0.05, the imaginary part was retrieved to 50% uncertainty. Simulations dealing with a mode-dependent complex refractive index showed that an average complex refractive index is derived that lies between the values for the two individual modes. Thus it becomes possible to investigate external mixtures of particle size distributions, which, for example, might be present along continental rims along which anthropogenic pollution mixes with marine aerosols. Measurement cases obtained from the Institute for Tropospheric Research six-wavelength aerosol lidar observations during the Indian Ocean Experiment were used to test the capabilities of the algorithm for experimental data sets. A benchmark test was attempted for the case representing anthropogenic aerosols between a broken cloud deck. A strong contribution of particle volume in the coarse mode of the particle size distribution was found. © 2004 Optical Society of America

OCIS codes: 010.1100, 010.3640, 290.1090, 290.5860.

1. Introduction

Aerosols are one of the key atmospheric constituents that influence the Earth's radiation budget and require a detailed characterization of optical and physical properties to reduce uncertainties in the modeling of the planet's radiative forcing.[1] Because of the highly variable lifetime of tropospheric aerosols of the order of days to weeks,[2] their inhomogeneous spatial distribution over the globe, as well as different source and transport paths, continuous monitoring is demanded. Satellite-based aerosol remote sensing provides for global coverage. Ground-based aerosol remote sensing is best suited for reliable and continuous monitoring of aerosol properties in key locations. Aerosol sounding with multiwavelength lidar in recent years has emerged as a powerful tool that is capable of providing comprehensive, quantitative information of aerosol properties on a vertically resolved scale.[3,4]

Techniques for the retrieval of microphysical particle parameters from multiwavelength lidar, developed since the early 1980s,[5–7] have made major progress in the past 5 years.[8–12] In that respect the most successful technique has been developed at the Institute for Tropospheric Research (ITR), Leipzig, Germany. It was developed initially for the retrieval of aerosol size distribution parameters and complex refractive indices from a multiwavelength Mie–Raman lidar that provides backscatter coefficients at six wavelengths and extinction coefficients at two wavelengths.[13] In recent years this tech-

nique has been further refined to make it usable for the limited data set of backscatter coefficients at three wavelengths and extinction coefficients at two wavelengths,[11,14] which, in principle, can be provided by a multitude of aerosol lidar systems operated throughout the world. These laser systems are based on a single Nd:YAG laser that is the most popular choice for investigation of aerosol particles. Although with a somewhat lower accuracy it has now become possible to derive the single-scattering albedo from the limited data set of such aerosol lidars. This quantity is one of the most important input parameters in the assessment of the influence of absorbing aerosols on climate change.

The necessity for long-term global monitoring of aerosol properties dictates the establishment of lidar networks. The first attempt at such a network was done with the Asian Dust Lidar Network (Murayama *et al.*, 2001),[15] which has been observing dust outbreaks from the Asian continents since 1997. From 1997 to 2000 the German Lidar Network[16] for the first time established an aerosol climatology over Germany on the basis of lidar observations. In 2000 the highly successful European Aerosol Research Lidar Network (EARLINET) became operational.[17] During the intensive period of this project from 2000 to 2003, 22 lidar stations in 13 European countries performed routine observations of aerosol properties. Quite obviously the enormous data set obtained from such networks would make them a prime candidate for detailed characterization of the physical particle properties. This idea has become more realistic since the inversion techniques that were originally designed to process the ITR six-wavelength aerosol lidar have been tuned to the processing of particle backscatter coefficients at three wavelengths and particle extinction coefficients at two wavelengths ($3\beta + 2\alpha$ data set). In principle, many of the lidar stations in EARLINET can provide for this reduced data set, because the lidar systems use a Nd:YAG laser as the light source.

In a recent publication[11] Veselovskii *et al.* described a modified version of Tikhonov's inversion[18] with constraints used for the retrieval of particle size distributions. In contrast to the classical Tikhonov's method, which accepts only that solution for which the discrepancy reaches its global minimum, in our algorithm we perform the averaging of solutions in the vicinity of this minimum. This averaging stabilizes the underlying ill-posed inverse problem. The classical Tikhonov method also demands *a priori* knowledge of optical data errors for the estimation of the stabilizing penalty term. Our use of the modified discrepancy eliminates the necessity for such information. The comparison of results obtained from $3\beta + 2\alpha$ data sets with simultaneous aircraft *in situ* measurements showed reasonably good agreement,[11] thus demonstrating the potential of using simplified multiwavelength Raman lidars in lidar networks.

The developed algorithm does not use any *a priori* assumption about the exact shape of the particle size distributions. In previous studies it has, however,

been applied only to monomodal logarithmic-normal particle size distributions. Particle size distributions normally consist of two modes in an optically active size range, denoted as the fine mode and the coarse mode. Extreme cases could occur along continental rims where marine and anthropogenic particles mix. Dust events could lead to the transport of large mineral particles into anthropogenically polluted areas. Hygroscopic growth could lead to comparably large particles.

Only a few studies up to now considered the retrieval of bimodal particle size distributions from lidar observations.[9,12] Studies were designed to determine the degree of separation of the two modes until the inversion breaks down.[9] Polynomials of high order were used to detect multimodal size distributions.[12]

The task of resolving structures that consist of coarse mode particles of ~ 10-μm radius is made more difficult by the fact that the longest wavelength available in routinely used lidars is 1.064 μm, and the fact that the corresponding kernel functions are not sensitive to size variations of such big particles. In our study we tried to answer the questions of whether the coarse mode of particle size distributions can be estimated from lidars based on one Nd:YAG laser and what uncertainties have to be expected.

In Section 2 we briefly describe the inversion algorithm. In Section 3 we present results from numerical simulations. We present measurement examples in Section 4 and conclude with a summary in Section 5.

2. Methodology

A. Inversion Code

Optical coefficients g_i of particles of spherical shape can be calculated as

$$g_i = \int_0^\infty K_i(m, r, \lambda) \frac{dn(r)}{dr} \, dr, \quad i = 1, \ldots, N_{\text{opt}}. \quad (1)$$

The quantity g_i summarizes the particle backscatter [$\beta(\lambda)$] and particle extinction [$\alpha(\lambda)$] coefficients, with N_{opt} being the number of available optical coefficients (α and β). The term $dn(r)/dr$ denotes the number concentration distribution. The expression λ describes the wavelength; $m = m_R - im_I$ is the complex refractive index, with m_R being the real part and m_I being the imaginary part; r is the particle radius; and $K_i(m, r, \lambda)$ are the kernel functions that are calculated from Mie theory for spherical particles. The size distribution in Eq. (1) can also be written in terms of surface-area $ds(r)/dr$ or volume $dv(r)/dr$ concentration. The corresponding kernel functions are obtained by dividing $K_i(m, r, \lambda)$ by $4\pi r^2$ and $(4/3)\pi r^3$, respectively, thus giving $K_{iS} = K_i/4\pi r^2$ and $K_{iV} = 3/4(K_i/\pi r^3)$. The volume kernel functions are usually used in the retrieval procedure.[5,6,8]

In a previous study[11] Veselovskii *et al*. did not find any significant influence of the kernel type on the retrieval results. In this study we repeated the sen-
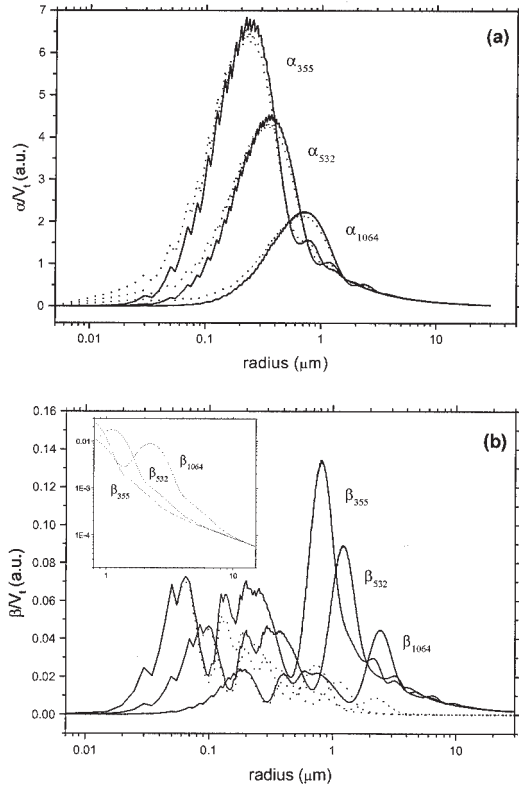
Fig. 1. Dependence of (a) aerosol extinction and (b) backscatter coefficients on particle size for wavelengths of 355, 532, and 1064 nm and refractive indices $m = 1.35 - i0$ (solid line) and $m = 1.35 - i0.02$ (dots). Coefficients α and β were obtained by integrating the Mie efficiencies over single-mode log-normal size distribution of width $\ln\sigma = 0.1$. The results are normalized to the particle total volume V_t. The inset in (b) shows the behavior of $\beta(\lambda)$ for $m = 1.35 - i.02$ in the radius range from 1 to 10 μm.

sitivity analysis with regard to the kernel functions as the size range for the inversion was extended toward larger sizes of 20 μm. Moreover, besides the traditionally used kernels, kernel functions of even higher order were constructed. These high-order kernels are calculated as

$$K_{i4} = \frac{K_i}{r^4}, \quad K_{i5} = \frac{K_i}{r^5} \ldots K_{ik} = \frac{K_i}{r^k}.$$

The retrieved particle size distributions have no simple physical interpretation, but $dn(r)/d\ln r$, $ds(r)/d\ln r$, and $dv(r)/d\ln r$ can be recalculated from them. The improvement in retrieval stability, which we can expect by changing number concentration kernels to surface, volume, or higher-order kernels, is related to the decrease of the contribution of big particles to backscattering. Figure 1 shows that the backscatter efficiency at different wavelengths from particles with $r > 3$ μm becomes comparably large, thus making the retrieval unstable. In the retrieval we integrate the kernel functions across the base functions,[11] which are wide enough to pick up the insensitive part of the kernels, corresponding to big radii. Dividing the kernels by r^k decreases the contribution of the big

particle radii, but at the same time raises the insensitive part of kernels at small particle radii. Hence we can expect that kernels of higher order will be better for the coarse mode estimation, even though they become less suitable for reproduction of the fine mode.

To solve the Fredholm integral equation (1) we use the same regularization approach as was done in a previous paper.[11] We briefly summarize the main steps. The solution $f(r)$ of Eq. (1), $[dn(r)/dr, ds(r)/dr$ or $dv(r)/dr]$, is approximated by the superposition of base functions $B_j(r)$:

$$f(r) \approx \sum_j C_j B_j(r) dr, \tag{2}$$

where C_j are so-called weight coefficients. The base functions have a triangular shape on an equidistant or a logarithmic-equidistant grid across the chosen radius interval in which the inversion is performed. The base functions are located next to each other and thus define a so-called inversion window $[r_{\min}, r_{\max}]$. The approximate values of the optical coefficients are then

$$g_i^\delta = \sum_{j=1}^{N_{bf}} A_{ij} C_j, \tag{3}$$

where N_{bf} is the number of base functions and A_{ij} is calculated as

$$A_{ij} = \int_{r_{\min}}^{r_{\max}} K_i(m, \lambda, r) B_j(r) dr, \tag{4}$$

where A_{ij} describes the so-called weight matrix. Representing C_j and g_i as vectors, the weight coefficients can be derived from the following relation[19]:

$$\bar{C} = (A^T A + \gamma H)^{-1} A^T g^\delta. \tag{5}$$

The expression γ denotes the Lagrange multiplier, and H is the smoothing matrix. A^T is the transpose of matrix A. The details for deriving Eq. (5) and the choice of Lagrange multiplier can be found in Refs. 8 and 11. In the previous version of our code the number of base functions N_{bf} coincided with the number of optical coefficients N_{opt}. In this version the code was modified to allow for a larger number of base functions than available data points. Because of the introduction of A^T into Eq. (5) the resulting matrices remain quadratic.

One of the problems that arise when dealing with large particles is the rapidly increasing computation time. In our first version of the program the kernels $K_i(m, r, \lambda)$ and matrix elements A_{ij} were recalculated for each inversion step. In the present version a data bank of Mie efficiencies was generated. The Mie efficiencies were calculated for particle radii from 0.01 to 20 μm in steps of 0.001 μm. The real part of the refractive index varied from 1.25 to 1.75 in steps of 0.025. The imaginary part varied from 0 to 0.05 in steps of 0.005. The use of this data bank strongly speeded up the computation times. The inversion of

Table 1. Typical Parameters of Bimodal Distribution of Different Types of Aerosol[a]

Aerosol Parameter	Urban Industrial	Biomass Burning	Desert Dust and Oceanic
r_f^v (μm)	0.14–0.18	0.13–0.16	0.12–0.16
r_c^v (μm)	2.7–3.2	3.2–3.7	1.9–2.7
$\ln \sigma_f$	0.38–0.46	0.4–0.47	0.4–0.53
$\ln \sigma_c$	0.6–0.8	0.7–0.8	0.6–0.7
V_f/V_c	0.8–2.0	1.3–2.5	0.1–0.5
m_R	1.4–1.47	1.47–1.52	1.36–1.56
m_I	0.003–0.015	0.01–0.02	0.0015–0.003

[a]r_f^v describes the volume radius in the fine mode of the particle size distribution; r_c^v is the volume radius in the coarse mode; $\ln\sigma_f$ and $\ln\sigma_c$ are the mode widths for the fine and coarse modes, respectively; V_f/V_c describes the ratio of volume in the fine and the coarse particle modes; m_R and m_I denote the real and the imaginary parts of the complex refractive index.

one data set with consideration of 4000 inversion windows takes approximately 20 min on a Pentium III PC but is still insufficient for routine lidar data processing. To speed the computations further, for the chosen kernel functions and number of base functions N_{bf} we generated the data bank of matrix elements A_{ij} according to Eq. (4). With the use of this data bank the inversion of one optical data set takes approximately 3 min.

B. Size Distributions

In the following simulations we used bimodal particle size distributions of the form

$$\frac{\mathrm{d}n(r)}{\mathrm{d}\ln(r)} = \sum_{i=f,c} \frac{N_{ti}}{(2\pi)^{1/2}\ln \sigma_i} \exp\left[-\frac{(\ln r - \ln r_i^n)^2}{2(\ln \sigma_i)^2} \right]. \quad (6)$$

The term N_{ti} is the total particle number of the ith mode, r_i^n describes the mode radius for number concentration distribution, and $\ln\sigma_i$ is the mode width of the ith mode. The index $i = f, c$ corresponds to the fine mode and the coarse mode, respectively. The same distribution can be written for volume $v(r)$ concentration, which is preferred, because in volume concentration representation both fine and coarse modes are relatively easy to distinguish. Both $\mathrm{d}n(r)/\mathrm{d}\ln r$ and $\mathrm{d}v(r)/\mathrm{d}\ln r$ have the same standard deviation σ and the relationships between radius and concentration for each mode are[20]

$$r_i^v = r_i^n \exp[3(\ln \sigma)^2], \quad (7)$$

$$V_{ti} = N_{ti}\frac{4}{3}\pi(r_i^n)^3 \exp\left[\frac{9}{2}(\ln \sigma)^2\right]. \quad (8)$$

For the simulation of bimodal size distributions different types of aerosol associated with different emission sources and mechanisms and optical properties have to be considered. Usually four main types of aerosol in the troposphere can be distinguished: urban industrial aerosol, biomass burning aerosol, desert dust, and marine origin aerosol. Table 1 shows the typical variability of the aerosol parameters for these aerosol types on the basis of

measurements with the worldwide Aerosol Robotic Network (AERONET).[21] Although the particle size distributions are not always bimodal for each measurement situation, as suggested by the numbers in Table 1, this parameter set represents a realistic approach to constraining the parameters for the simulations presented here.

The radii of the fine mode and the coarse mode as well as the refractive indices vary strongly within each aerosol type. The variation between the different types of aerosol is similarly strong. The main difference between the aerosol types is the ratio of the volume of the fine mode to the coarse mode. For urban industrial and biomass burning aerosols the fine fraction prevails for dust and marine aerosols the volume of the coarse mode by far exceeds the volume of the fine mode. Examples for particle parameters used in climatology calculations are presented in Ref. 22. An extensive literature on particle properties, mostly derived from *in situ* observations, can also be found in special issues on the Tropospheric Aerosol Radiative Forcing Observational Experiment,[23,24] the Aerosol Characterization Experiment (ACE) 2,[25] the Indian Ocean Experiment (INDOEX),[26] the Asian Pacific Regional Aerosol Characterization Experiment,[27] and the Lindenberg Aerosol Characterization Experiment.[28]

Although the particle size distributions for Asian dust and marine aerosols are similar, there is an important difference: marine aerosols can be considered spherical under most situations such as the high relative humidity that generally prevails over water, whereas dust particles are irregular in shape. In our study we consider only spherical particles, and the possibility to extend the results obtained here to nonspherical particles is beyond the scope of this paper.

Based on the results presented in Ref. 22, we consider two types of particle size distribution, denoted as type I and type II. Type I has the following parameters: $r_f^v = 0.15$ μm, $\ln \sigma_f = 0.4$, $r_c^v = 2.7$ μm, $\ln \sigma_c = 0.6$, and $V_{tf}/V_{tc} = 2$. In that case the fine mode is dominant. This distribution describes industrial and biomass burning aerosols. Type II has the same parameters except for $V_{tf}/V_{tc} = 0.2$, which means that the main part of the aerosol volume is presented by the coarse mode. This distribution describes marine aerosols. The refractive index was assumed to be mainly $m = 1.45 - i0.015$ for both modes. We also present results for other complex refractive indices and the important case in which the refractive indices of the fine and coarse modes differ.

In the current study we pursued several goals. We performed numerical simulations to determine how the stability of the inversion depends on errors in the optical data, on the type of kernel functions, on the number of optical data and base functions, and how the averaging procedure works for the bimodal particle size distribution. We also considered the situation in which fine and coarse aerosol modes have different refractive indices. The simulations were

performed mainly for the data set of 3β and 2α, because we intend to demonstrate that this simplified version of lidar can be used to estimate the parameters of the particle size distribution with the accuracy superior to within the range of natural variation of aerosol parameters listed in Table 1.

3. Numerical Simulations

A. Analysis of Optical Spectra

To estimate the maximum particle radii that can be retrieved from measurements with a triple Nd:YAG laser we first investigated volume backscatter and extinction coefficients at 355-, 532-, and 1064-nm wavelengths as a function of particle size. Figure 1 shows the results of the calculation for the complex refractive index $m = 1.35 - i0$. Short-term oscillations of the corresponding Mie efficiencies are not relevant for the following discussion. These oscillations were smoothed by integrating them over monomodal logarithmic-normal size distributions of mode radius r_0 and mode width $\ln\sigma = 0.1$. The coefficients α_λ, β_λ obtained in this way were normalized to the particles' total volume V_t by use of Eqs. (7) and (8). The backscatter coefficients β_{532}, β_{1064} become practically indistinguishable for $r_0 > 3\ \mu m$, which thus represents the upper limit of the resolvable particle radius range. Similar results were found by Heintzenberg et al.[5] and Donovan et al.[29]

The size distributions listed in Table 1 have their maximum value of dv/dr in the coarse mode at $r_0 \approx 2\ \mu m$, hence the coarse fraction of the particle size distribution contributes differently at 355 and 1064 nm. Calculations performed for type I aerosols with $m = 1.45 - i0.015$ demonstrate that the contribution to total backscatter is 18% at 1064-nm and 2.5% at 355-nm wavelengths. The method should fail when the contribution of the coarse mode to total scattering at 1064 nm becomes comparable with the measurement error of the optical data, which can be kept as low as 10% for Raman lidar. For the chosen distribution it corresponds to a ratio of $V_{tf}/V_{tc} \approx 4$. Extinction coefficients at 355- and 532-nm wavelengths differ strongly for small radii, allowing us to distinguish particle sizes as small as 0.05-μm radius.

The inverse problem defined by Eq. (1) is especially difficult to solve because of the high sensitivity of the particle scattering properties with respect to the complex refractive index. The dotted curves in Fig. 1 show the same coefficients calculated for $m = 1.35 - i.02$. An increase of the imaginary part of the refractive index does not noticeably change extinction for $r > 0.1\ \mu m$, but only for $r < 0.1\ \mu m$. In contrast, for backscattering the rise of m_I decreases β for big radii. It is interesting that backscatter, although weaker for larger m_I, is distinct for different wavelengths almost up to 10 μm, thus allowing retrieval to larger radii. Figure 2 shows β/V_t and α/V_t at $\lambda = 1064$ as a function of particle size for different values of m_R. Changing m_R from 1.35 to 1.5 enhances the maximum of β/V_t by a factor of 3. On the one hand the high sensitivity of β with regard to variations of
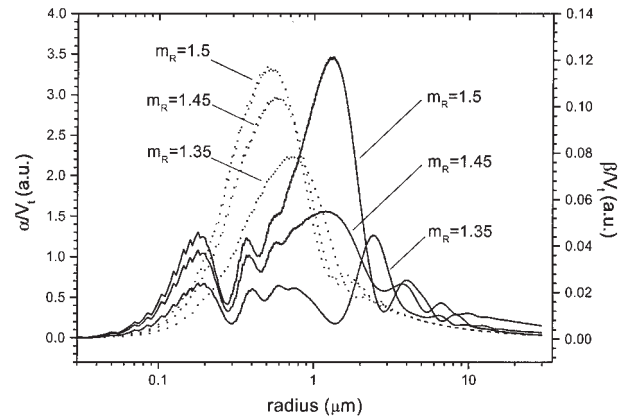

Fig. 2. Dependence of particle backscatter (solid) and particle extinction (dot) coefficients at $\lambda = 1064$ nm on particle radius for $m = 1.35 - i0$, $m = 1.45 - i0$, and $m = 1.5 - i0$. The results are normalized to the total volume V_t of the particles.

m_R and m_I provides a good basis for the retrieval of the complex refractive index from the lidar data. On the other hand it represents one source of the instability of the algorithm. In contrast with the backscatter coefficients the extinction coefficients do not depend that much on m_R and remain rather unchanged with respect to variations of m_I. The combination of α and β, as was shown previously,[9,11] allows us to reach a compromise, i.e., the procedure remains rather stable and retrieval of the complex refractive index is still possible.

Variation of the scattering properties becomes more complicated for the bimodal size distribution. Figure 3 shows the dependence of α and β on m_R at $\lambda = 355$, 532, and 1064 nm for type II aerosol with $N_t = 10^3\ cm^{-3}$. The backscatter coefficient at 1064 nm can be higher or lower than the one at 532 nm depending on m_R, whereas the extinction coefficients at 355 and 532 nm change monotonically. Hence the combination of α and β should also stabilize retrieval in the case of bimodal size distributions.
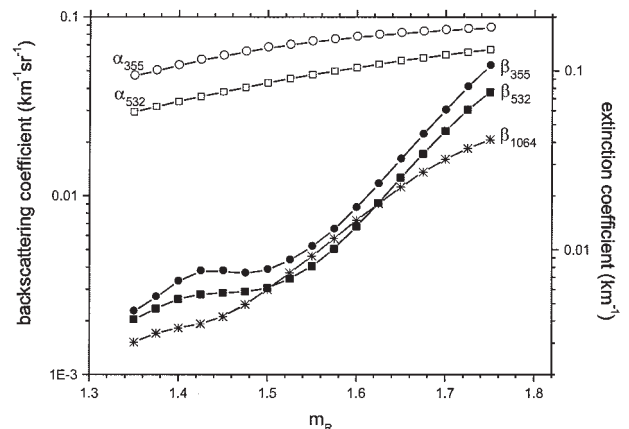

Fig. 3. Dependence of particle backscatter and particle extinction coefficients at 355-, 532-, 1064-nm wavelengths on the real part of the refractive index for type II aerosol. The imaginary part of refractive index $m_I = 0$.
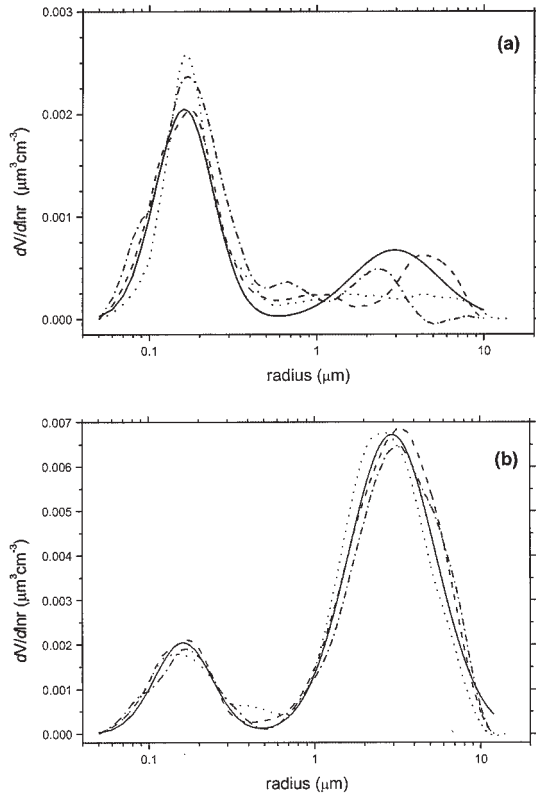
Fig. 4. Retrieval of volume size distribution for (a) type I and (b) type II aerosols. Simulations were performed for $3\beta + 2\alpha$ (dash, dot) and $6\beta + 2\alpha$ (dash–dot) data sets using volume kernel functions. Refractive indices $m = 1.45 - i0.015$ (dash, dash–dot) and $m = 1.65 - i0.015$ (dot) were assumed unknown. Optical data were free of errors. Solid line represents the initial bimodal particle size distribution.

Fig. 5. Volume size distribution for known (dot) and unknown (dash, dash–dot) refractive index $m = 1.45 - i0.015$. Simulations were performed for $3\beta + 2\alpha$ (dash) and $6\beta + 2\alpha$ (dot, dash–dot) data sets using volume kernel functions. Optical data were free of errors. The solid line represents the initial bimodal particle size distribution. Results obtained with known m for the $3\beta + 2\alpha$ data set are close to the results obtained with the $6\beta + 2\alpha$ data set.

B. Inversion

1. Error-Free Data

The first test consisted of retrieval of the initial bimodal particle size distribution in the absence of optical data errors. Figure 4 shows the inversion results for $3\beta + 2\alpha$ and $6\beta + 2\alpha$ data sets for type I and type II aerosols, respectively. The refractive indices were $m = 1.45 - i0.015$ and $m = 1.65 - i0.015$ for each case considered here. Volume kernel functions were used, and the solutions were averaged in the vicinity of the discrepancy minima; the criterion of choosing the averaging interval will be discussed below.

It is interesting to note that the parameters retrieved from the $6\beta + 2\alpha$ data set do not provide an accuracy superior to the results obtained from the inversion of the $3\beta + 2\alpha$ data set. The use of additional backscatter coefficients inside the spectral interval from 0.355 to 1.064 μm does not improve the reproduction of the particle coarse mode. An improvement can be achieved only with the use of longer wavelengths. Unfortunately the calculation of β from lidar data with an accuracy of 10% in the infrared wavelength range meets significant difficulties. Moreover, for such wide spectral ranges the wave-
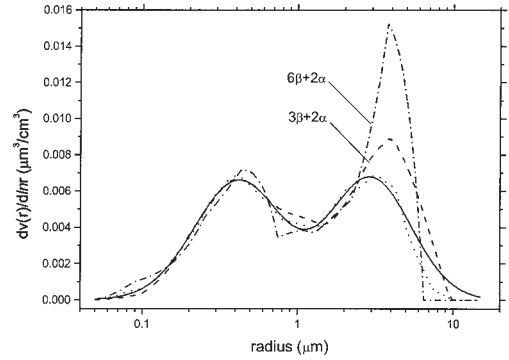
length dependence of the particle refractive index must be taken into account.

The retrieval of type II particle size distributions is more stable, because the coarse mode contributes 70% to the total backscatter coefficient at $\lambda = 1064$ nm for $m = 1.45 - i0.015$. The retrieved particle size distribution almost coincides with the initial one for both values of the refractive indices. For type I particle size distributions the reproduction of the coarse mode is poor (its contribution to total backscatter is only 18% for the same wavelength and refractive index), but the contribution of particles in that mode to total volume is low, so it does not lead to serious errors in the parameter estimation.

Figure 5 shows the more difficult situation when fine and coarse modes of the particle size distribution are comparable. This distribution is obtained from type II by keeping the same coarse mode and increasing radius and dispersion of the fine mode to $r_f^v = 0.41$ μm and $\ln\sigma_f = 0.65$, respectively. In this case the contribution of the coarse mode to total backscatter at 1064 nm is 28%.

When refractive index $m = 1.45 - i0.015$ is assumed known, the initial particle size distribution is well reproduced from both $3\beta + 2\alpha$ and $6\beta + 2\alpha$ data sets. But for unknown m the uncertainty of the retrieved coarse mode is enhanced. The errors of estimation N_t, S_t, V_t, and r_{eff} for $3\beta + 2\alpha$ ($6\beta + 2\alpha$) sets are, respectively, 30% (37%), 3% (8%), 9% (16%), and 11% (7%).

2. Averaging of Solutions

Errors in the optical data create instabilities in the inversion. The additional stabilization of the procedure is achieved by averaging solutions near the minimum of the discrepancy ρ_{min}.[11] In a previous paper[11] Veselovskii *et al.* demonstrated that the uncertainty of the retrieved parameters for monomodal particle size distributions does not depend significantly on the choice of averaging interval $[\rho_{min}, \rho_{max}]$.
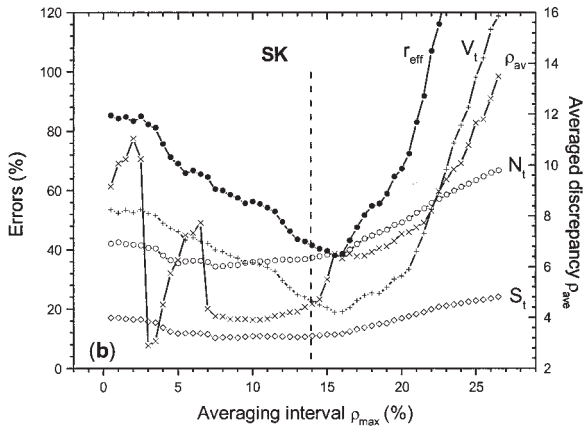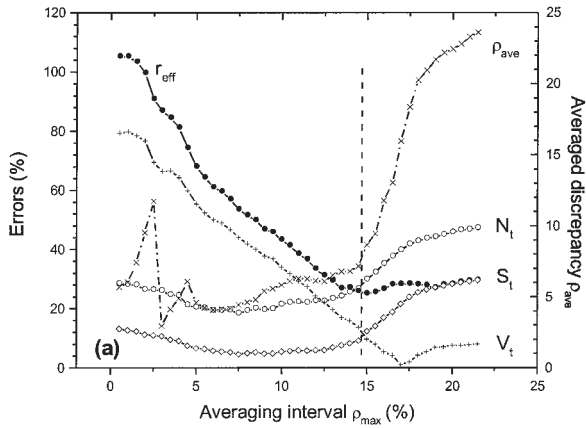
Fig. 6. Errors of estimation of number (N_t), surface (S_t), volume (V_t) concentration, particle effective radius r_{eff}, and averaged discrepancy ρ^{ave} as a function of averaging interval ρ_{max}. For the inversion of the $3\beta + 2\alpha$ data set the (a) volume and (b) surface area kernel functions were used. The error of the optical data is 10%. The dashed line represents the chosen interval of averaging.

Usually averaging is performed over the interval in which 10% of the solutions are concentrated. For bimodal particle size distributions with their large particle radii the correct choice of averaging interval becomes more critical. Therefore we improved the criterion for determining ρ_{max} according to the discrepancy of averaged solutions ρ^{ave}, determined as

$$\rho^{ave} \equiv \frac{1}{N_{opt}} \sum_i \left| \frac{g_i - g_i^{ave}}{g_i} \right| .$$

The term g_i again denotes the measured optical coefficients, and g_i^{ave} are the coefficients calculated from the solutions averaged in the interval [ρ_{min}, ρ_{max}].

Figure 6 illustrates the choice of the averaging interval based on the use of the averaged discrepancy ρ^{ave}. Shown are N_t, S_t, V_t, r_{eff}, and ρ^{ave} as functions of the averaging interval ρ_{max}. The calculations were performed for type II aerosols with $m = 1.45 - i0.01$ and using surface and volume kernel functions. The error of the $3\beta + 2\alpha$ data set was 10%. On the basis of results from numerous simulations we con-
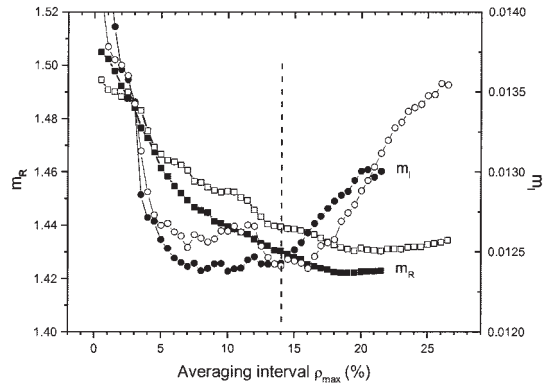

Fig. 7. Real (squares) and imaginary (circles) parts of the complex refractive index calculated with volume (filled symbols) and surface area (open symbols) kernels as a function of averaging interval ρ_{max}. The data set is the same as in Fig. 6. The initial refractive index is $m = 1.45 - i0.01$. The dashed line represents the chosen interval of averaging.

clude that the best parameter estimation is achieved for that averaging interval for which the averaged discrepancy ρ^{ave} becomes stable (it may oscillate around some constant level) and averaging is stopped before the discrepancy ρ^{ave} starts to rise.

Figure 6(a) shows the dependence of ρ^{ave} on ρ_{max} on the basis of the volume kernel functions. There is a fast rise of ρ^{ave} for $\rho_{max} > 14\%$, so we chose this value as the averaging interval. After averaging there is a significant decrease of the estimation uncertainty. For effective radius the error decreases from 105% to 27%, and for volume concentration the error decreases from 80% to 16%. Number and surface-area concentration are less affected by the averaging interval in the present case. Simulations with other data sets however also demonstrated a strong dependence on ρ_{max} in some cases. Although the uncertainty for the different parameters may become a minimum for different values of ρ_{max} the averaging interval chosen in this way in general presents a reasonable compromise.

Figure 6(b) shows the dependence of the inversion results on the averaging interval for the case of surface-area kernels. The dependence of the averaged discrepancy ρ^{ave} on ρ_{max} becomes more oscillatory, which complicates the choice of averaging interval. For the data set considered here the particle parameters retrieved with the surface kernels show a higher uncertainty compared with the results shown in Fig. 6(a). However a clear preference of volume kernel functions over surface-area kernel functions is not given. In some cases surface-area kernel functions gave better results than volume kernel functions. A slight improvement of the inversion is observed if both kernel types are used and corresponding results are averaged.

Figure 7 shows the dependence of the real and imaginary parts of the refractive index on the averaging interval for the same data set shown in Fig. 6. The results obtained with the surface-area and volume kernel functions are quite similar, i.e., $m =$
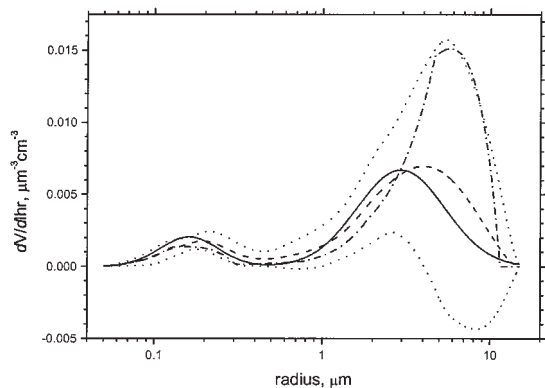
Fig. 8. Effect of averaging of solutions on the basis of five base functions. Shown is the solution corresponding to the minimum discrepancy (dash–dot), the averaged solution (dashes), and the initial bimodal distribution (solid curve). The data set is the same as in Fig. 6. The dotted curves indicate the mean-square deviation of the individual solutions used for the calculation of the average value.

Table 2. Errors of Estimation of Aerosol Total Number (N_t), Surface (S_t), Volume (V_t) Concentration, and Effective Radius (r_{eff})[a]

Kernel Types	N_t (%)			S_t (%)			V_t (%)			r_{eff} (%)		
NK	15	35	60	15	10	10	25	30	20	35	20	35
SK	30	70	30	15	35	10	20	35	40	30	50	45
VK	50	100	40	30	35	10	20	30	30	35	50	10
K-4	140	160	120	50	60	30	10	30	25	40	55	15
K-5	200	210	180	60	75	50	10	55	15	50	75	40

[a]Results obtained with number (NK), surface area (SK), volume (VK), fourth-(K-4), and fifth-(K-5) order kernels for three different program runs. Error of the $3\beta + 2\alpha$ data set was 20%.

$1.43 - i0.0125$ for volume kernels and $m = 1.44 - i0.0125$ for surface-area kernels.

An overestimation of the complex refractive index, if the solution at the minimum of the regularization curve is taken, has been reported in previous studies of a similar version of the inversion code presented here.[9] Also in the present case we observe an overestimation of m corresponding to the minimum discrepancy, but after averaging both, the real part as well as the imaginary part of the refractive index come rather close to the initial value of $1.45 - i0.01$.

Figure 8 illustrates the effect of averaging solutions on the retrieved shape of the size distribution. Shown is the solution that corresponds to the minimum of discrepancy, the averaged solution, and the initial bimodal particle size distribution. The data set used is the same as in Fig. 6. The dotted lines indicate the mean-square deviation of the individual solutions from the average value. The deviation is calculated in the same way, as is described in Ref. 11. The coarse mode of the solution, corresponding to the minimum of discrepancy, significantly exceeds the initial one, but the averaging procedure significantly improves the reconstruction of the coarse mode.

As mentioned before, we considered different types of kernel function as they might determine the stability of the inversion. In a previous paper[11] that dealt with monomodal particle size distributions, no significant difference was found with respect to the choice of different kernel functions. In the current study number, surface-area, volume, fourth- (K_{i4}) and fifth- (K_{i5}) order kernel functions were tested. Simulations were performed for $3\beta + 2\alpha$ data sets of type II aerosol with 20% data error. Table 2 shows the accuracy of the parameter estimation with different kernel functions obtained during three program runs.

There is a significant spread among the individual solutions as can be seen from the result of three individual runs. As mentioned before, the inversion results depend strongly on the error distribution between the optical coefficients and this should be kept in mind when discussing the dependence of parameter uncertainties on different kernel types. Another important result, as already mentioned in the discussion of Figs. 6 and 7, is that different parameters are retrieved best at different values of ρ_{max}, and the choice of the averaging interval is always the compromise of uncertainties of these parameters relative to each other. Usually the best estimations of number concentration are obtained with low-order kernels (number or surface area) and the best estimates of volume are obtained with volume and fourth-order kernels. Fifth-order kernels usually already lead to the degradation of accuracy.

The solutions corresponding to the minimum of discrepancy obtained with number density kernels differ strongly from the initial value and are more oscillatory. After averaging the accuracy of parameter estimation with number kernels becomes comparable with the results obtained for surface and volume kernels, although the size distribution itself is reproduced less well. Moreover, the results obtained with number kernels are more sensitive to the choice of the averaging interval, thus leading to additional uncertainty. For that reason we do not consider number kernels to be attractive for routine data processing. The best compromise is achieved with the use of surface or volume kernels. The parameter estimation improves when the mean of the values obtained with surface and volume kernels, respectively, is taken. This averaging of kernels should be further investigated, so that it might become part of data retrieval strategy in a future version of the code. The complex refractive indices calculated with different kernels are quite close. The deviation of m_R from the initial value did not exceed ± 0.05, and the deviation of m_I did not exceed 50%.

Figure 9 shows the particle size distributions obtained with the five different kernel functions used in this study and for 20% data error. The general tendency is the increase of the mean radius r_0 of the coarse mode with the rise of the order of the kernel functions. In the present example the kernels of higher order improve the reproduction of the coarse mode, whereas the reproduction of the fine mode degrades. Other program runs showed that the evolution of the particle size distribution, depending on
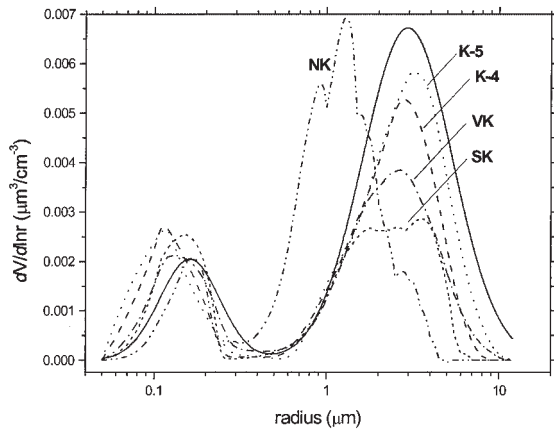
Fig. 9. Volume concentration distribution retrieved with number (NK), surface area (SK), volume (VK), fourth- (K-4) and fifth- (K-5) order kernel functions. The solid curve represents the initial bimodal distribution. The error of the data set is 20%.

the rise in kernel order, is not necessarily as smooth as shown in Fig. 9. In general surface-area and volume kernels again are best suited as they permit a reasonable compromise in the reproduction of fine and coarse modes.

3. Dependence on Number of Base Functions

Another test dealt with the stability of the inversion depending on the number of base functions. Tests showed that base functions distributed along a logarithmic radius range always lead to better retrieval results compared with base functions spread along a linear radius range. Therefore the following simulations are based on the use of the logarithmic radius range.

Figure 10 shows the results of the retrieval of volume concentration distributions $dv(r)/d\ln r$ of type II aerosols for 5, 8, and 12 base functions on the basis of data sets of $3\beta + 2\alpha$. The retrieval was performed with volume kernel functions. The complex refractive index $m = 1.45 - i0.01$ was assumed unknown. The solutions obtained were averaged as described in
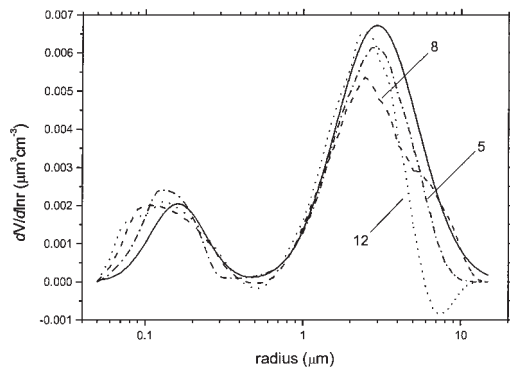

Fig. 10. Size distribution retrieved with different numbers of base functions: 5 (dash–dot), 8 (dash), and 12 (dot). Solid curve represents the initial size distribution. Volume kernels were used. The data set consisted of $3\beta + 2\alpha$ with a 10% error. The complex refractive index was assumed unknown during inversion.

Subsection 3.B.2. The averaging interval was optimized for each number of base functions, thus allowing this comparison. In the case of error-free optical data, for which the results for the different number of base functions did not differ significantly, the retrieved size distributions were close to the initial size distribution. Differences became obvious after errors, in this case 10%, were introduced. Figure 10 shows that the increase of the number N_{bf} of base functions does not improve the accuracy. The best results were obtained for a number of base functions equal to the number of optical data. For $N_{bf} = 5$, the accuracy of V_t, S_t, and N_t is 12%, 20%, and 52%, respectively. The accuracies of the same parameters for $N_{bf} = 8$ are 13%, 32%, and 110%. $N_{bf} = 12$ gives accuracies of 18%, 45%, and 150%. Simulation for type I aerosols leads to a similar conclusion, i.e., the number of base functions should be equal to the number of optical data. The result of keeping N_{bf} low and yet obtaining smooth particle size distributions can be explained in two ways: It is quite obvious that a low number of base function presents a rather strong constraint on the solution finding, i.e., the lower the number of base functions the lower the degrees of freedom in the inversion. Second, a low number of base functions can only give a crude resolution of the shape of the particle size distribution. This effect, however, is compensated for by averaging many solutions in the vicinity of the minimum discrepancy, which leads to the smoothing of the mean solution.

4. Method Accuracy

Errors in the optical data set were introduced in a random way. For a realistic estimation of the method uncertainty we performed the procedure ten times for each type of aerosol. The maximum observed error was considered as the method accuracy. The simulations were performed with surface-area and volume kernels, and the mean values of the parameters obtained in this way were taken. Table 3 summarizes the results for the $3\beta + 2\alpha$ data sets and 10% optical data errors. Type II aerosols are characterized by higher errors in volume concentration and effective radius compared with the results for type I aerosols. These results can be explained by the fact that the main part of the volume of type II aerosols is contained in the coarse mode. The retrieval of the coarse mode however is less stable compared with the retrieval of the fine mode. In contrast, uncertainties of number and surface-area concentration are smaller for type II aerosols. Taking the mean value of the results obtained with two types of kernel leads to some improvement of the parameter estimation, which is especially noticeable for the calculation of N_t. If no *a priori* information on the aerosol type is available, the inversion of experimental lidar data would therefore have to be assumed to be as large as $\varepsilon_{Nt} = 70\%$, $\varepsilon_{St} = 40\%$, $\varepsilon_{Vt} = 45\%$ and $\varepsilon_{reff} = 40\%$. The accuracy of the complex refractive index did not depend significantly on the kernel type. For the real part m_R the uncertainty

Size Distribution	N_t (%)		S_t (%)		V_t (%)		r_{eff} (%)		m_R	m_I (%)
	VK	VK + SK	VK	VK + SK	VK	VK + SK	VK	VK + SK		
Type I	90	70	50	40	25	25	40	40	±0.05	50
Type II	60	40	17	15	45	45	55	40	±0.05	50

[a]Errors of optical data are 10%.   Table shows results for volume kernels (VK) and mean of values obtained with volume and surface area kernels (VK + SK).

always was within ±0.05.   The uncertainty of m_I did not exceed 50%.

Figure 11 illustrates the scattering with respect to the shape of the particle size distributions obtained from ten program runs for type I and type II aerosols, respectively.   The data set was 3β + 2α, and the uncertainty was set to 10%.   The oscillations of the solutions at big radii determine the limit of detecting the coarse mode.   For type II particle size distributions the parameters of the coarse mode (r_{02}, σ_2) can be estimated.   For type I aerosols the scattering of the solutions is strong and does not allow for a good reconstruction of the coarse mode.

As mentioned in Section 2 the method of finding the averaging interval was modified from the technique used for the retrieval of monomodal particle size distributions.[11]   Figure 12 shows that this modified approach of solution finding also works well for monomodal size distribution, i.e., when the coarse mode is absent.   Simulations were performed for the same parameters as used in Fig. 11.
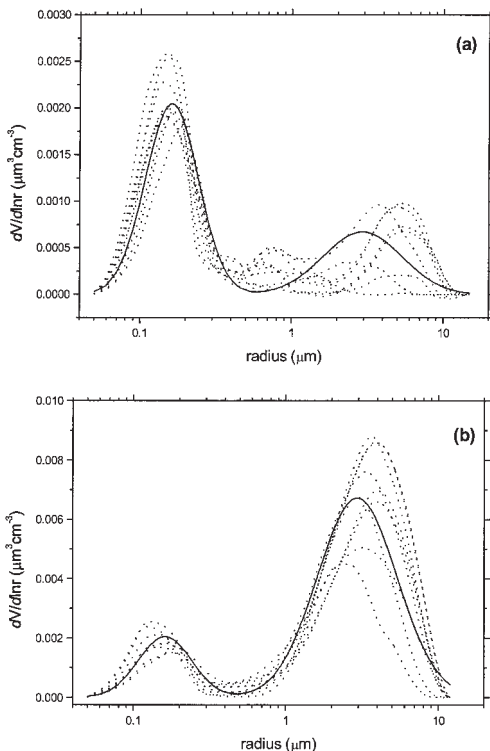
The retrieval of the complex refractive index becomes difficult for big particles, that is, for radii above ~2 μm, because the backscatter coefficients for different refractive indices become rather similar, as can be seen from Fig. 2.   To study the retrieval uncertainties for such big radii we performed simulations for a size distribution with parameters of the coarse mode of $r_c^v = 5.3$ μm and $\ln\sigma_f = 0.6$.   The fine mode was kept the same as for type II aerosol.   The effective radius of such a distribution is approximately 2.25 μm.   The results of the retrieval for a 3β + 2α set with volume kernels are presented in Fig. 13.   The simulation was carried out for $m = 1.35 - i0$, which describes the case of aerosols with a comparably high concentration of water or the case of pure water clouds.   For the aerosol size distribution considered here, the backscatter coefficients at 532 and 1064 nm differ by less than 5%, so even in the absence of optical data error the uncertainties of the retrieved parameters are significant.   The retrieved refractive index is $m = 1.44 - i0$ and is thus higher than the initial one.   The uncertainties of N_t, S_t, V_t, and r_{eff} are 29%, 15%, 34%, and 27%, respectively. Introducing 10% optical data errors increases the uncertainties even more.   For the present example the uncertainties are 51%, 15%, 57%, and 51%, and the retrieved refractive index is $1.51 - i0$.

The precision of inversion is improved if the refractive index corresponding to water is assumed.   For known m and the same data set with 10% error the uncertainties become 68%, 14%, 14%, and 24%, which significantly improves the accuracy of the retrieved coarse particle mode.

Fig. 11.   Uncertainty of size distributions for ten runs of (a) type I and (b) type II aerosol retrieval.   The 3β + 2α optical data were inverted with volume kernels and had a 10% error.
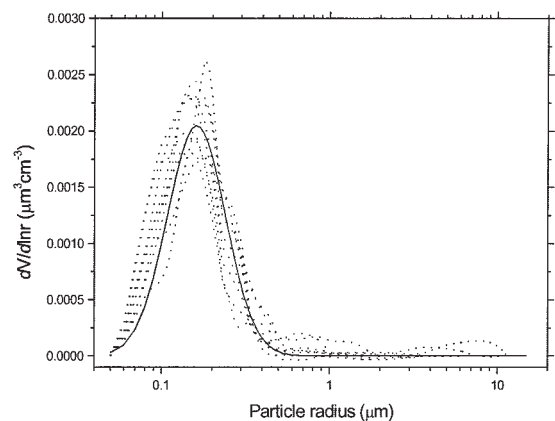

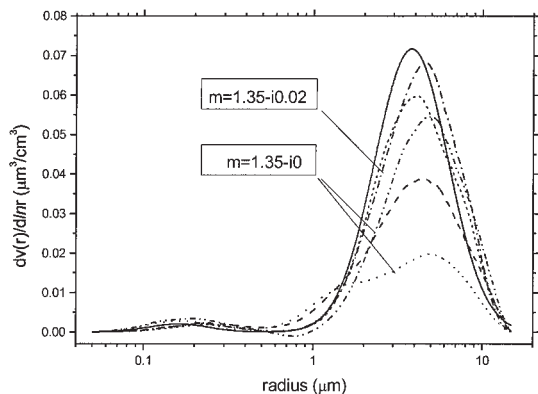Fig. 12.   Same as Fig. 11 but for a monomodal particle size distribution.

Fig. 13. Volume size distributions for the refractive indices of $m = 1.35 - i0$ (dot, dash, dash–dot–dot) and $m = 1.35 - i0.02$ (dash–dot, short dash), and the use of volume kernels. Simulations were done for the case of error-free data (dash–dot, dash), and data errors of 10% (short dash, dot, dash–dot–dot) for a $3\beta + 2\alpha$ data set. The solid curve represents the initial bimodal particle size distribution. The dash–dot–dot curve represents the result for a data error of 10% and a known refractive index of $m = 1.35 - i0$.

It is interesting that the accuracy improves if the imaginary part of the refractive index is increased. This result might be anticipated from calculations presented in Fig. 1, showing that for $m_I = 0.02$ the backscattering at 532 and 1064 nm for big radii becomes different. For $m = 1.35 - i0.02$ and in the absence of data errors, the retrieved distribution practically coincides with the initial size distribution, and the retrieved refractive index is $1.36 - i0.02$. Even for a data error of 10%, the retrieval is stable, the uncertainties of N_t, S_t, V_t, and r_{eff} are 52%, 16%, 7%, and 10%, respectively, and $m = 1.37 - i0.02$. The main criterion, that the retrieval is still credible, is the ratio $|\beta_{532} - \beta_{1064}|/\beta_{532}$, which has to be larger than 10% if the measurement error is of that order of magnitude.

5. Size Dependence of the Complex Refractive Index

The simulations presented so far assumed that fine and coarse modes have the same complex refractive index, although in reality these might differ. This effect is more significant for type II aerosols, in which the coarse mode contributes strongly to the total scattering. Only a few studies on size-dependent complex refractive indices of bimodal distributions have been made so far.[9] These studies focused on characterizing the stability of the inversion code for various situations of a size-dependent complex refractive index. In the study presented here we present for the first time to our knowledge a quantitative evaluation of the properties of the inversion code for size-dependent complex refractive indices.

Figure 14 illustrates the influence of a size-dependent refractive index on the retrieved particle size distribution. Shown are size distributions obtained from an error-free $3\beta + 2\alpha$ data set and different combinations of m_f and m_c. For $m_f = 1.55 -$
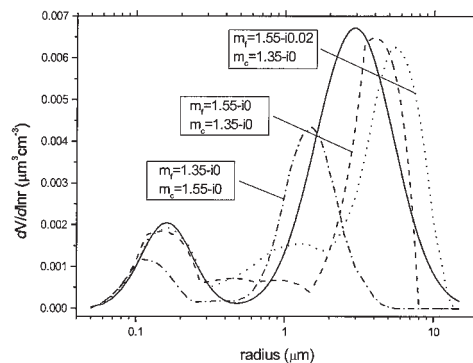

Fig. 14. Retrieval of size distribution with different refractive indices in the fine (m_f) and the coarse (m_c) modes. For inversion of the $3\beta + 2\alpha$ data set volume kernel functions were used. Optical data were error free. The solid curve represents the initial size distribution.

$i0$ and $m_c = 1.35 - i0$ the coarse mode of the retrieved particle size distribution is shifted to large radii. This shift becomes even stronger when we increase the imaginary part of m_f from 0 to 0.02. In the case of $m_c > m_f$, i.e., $m_f = 1.35 - i0$ and $m_c = 1.55 - i0$, the retrieved particle size distribution is shifted to smaller radii.

To estimate the uncertainty introduced by size-dependent refractive indices we performed simulations for type II aerosols using $3\beta + 2\alpha$ data sets with 10% errors. Calculations were performed for two combinations of m_f and m_c. In the first case we used $m_f = 1.55 - i0.01$ and $m_c = 1.35 - i0$. In the second case we used $m_f = 1.35 - i0$ and $m_c = 1.55 - i0.01$. The refractive index of the absorbing component can be interpreted as moderately absorbing anthropogenic aerosol, whereas the nonabsorbing component can be interpreted as particles of marine origin. For each combination the program was run ten times and the worst-case situation was taken as quality criterion, i.e., the maximum uncertainty obtained for each parameter from the twenty runs, respectively, was considered as the final accuracy. The uncertainties of r_{eff}, N_t, S_t, and V_t are 55%, 60%, 30%, and 50%, respectively. In general these errors do not exceed the errors listed in Table 3, except for S_t, which increased from 17% to 30%.

Figure 15 illustrates the scattering of the shape of the particle size distribution obtained from the ten program runs. Shown is the result for $m_f = 1.55 - i0.01$ and $m_c = 1.35 - i0$. The mean radii of the retrieved coarse modes are shifted to bigger radii compared with the given one. The amplitude of the coarse mode shows large variations. In summary we can conclude that even in the case of bimodal particle size distribution consisting of different complex refractive indices and 10% data error there is reasonable parameter estimation.

4. Measurement Example

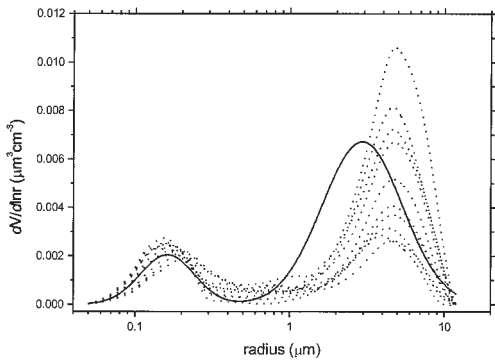The simulations described above dealt with the detection of large particles in bimodal particle size dis-

Fig. 15. Retrieval of the size distribution for $m_f = 1.55 - i0.01$ and $m_c = 1.35 - i0$. The optical data errors were 10%. Dotted curves represent the scattering of solutions obtained in ten program runs. For inversion of the $3\beta + 2\alpha$ data set volume kernel functions were used. The solid curve represents the initial size distribution.

tributions. The algorithm therefore was further tested for two experimental data sets describing the presence of large particles. The data were taken from a measurement carried out during the INDOEX (Ramanathan *et al.*, 2001).[30] Table 4 shows the spectra of the backscatter coefficients and extinction coefficients used in this study. The measurement example represents anthropogenic pollution observed on 7 March 1999, when air was advected to the field site from Southeast Asia. Details of this measurement can be found in Refs. 3 and 31.

The measurements were done with the ITR six-wavelength lidar.[13] The system emits laser pulses at 355, 400, 532, 710, 800, and 1064 nm. For the aerosol retrieval presented here we used the back-scattered light detected at the laser wavelengths and the Raman signals of nitrogen at 387 nm (355-nm primary wavelength) and 607 nm (532-nm primary wavelength). The two nitrogen Raman signals at 387 and 607 nm were used for the computation of profiles of the particle extinction coefficients at 355 and 532 nm.[32–34] The elastic backscatter signals and the corresponding signals from Raman scattering by nitrogen molecules were used for the retrieval of profiles of the backscatter coefficients at 355 and 532 nm with the Raman-lidar method.[33,34] The particle backscatter coefficients at 400, 710, 800, and 1064 nm were calculated with the so-called Klett

method[35] from the elastic backscatter signals by use of variable lidar ratios obtained at 355 and 532 nm with the Raman method.

Two height ranges are considered in the analysis. In the height range from approximately 600–1000 m trade cumulus clouds were observed. In contrast, the height range from 1325 to 1650 m was cloud free. The data used here were cloud screened, thus leaving only the information on the pure particle signal. However, because of the high relative humidity, in particular at the height range at which clouds were observed, it is most likely that a portion of the signal in the lower height range is still affected by traces of droplets, or that the observed particles contained a large fraction of water as the result of hygroscopic growth. For that reason it is most likely that next to the fine particle mode, originating from small anthropogenic particles, a second coarse mode was present in the particle size distribution.

The numbers were derived on the basis of data set $6\beta + 2\alpha$, and once more for the reduced data set $3\beta + 2\alpha$. Table 4 shows that two different values for the particle backscatter coefficient at 1064 nm were used. The different values take particular account of the comparably large uncertainty, which is involved in the retrieval of this parameter. The inversion results for 600–1000- and 1325–1650-m layers are given in Tables 5 and 6 respectively. For the analysis we used both values for the backscatter coefficient at 1064 nm.

The inversion of the $6\beta + 2\alpha$ data set yields an effective radius of 0.34 ± 0.13 μm. Consideration of the lower value for β_{1064} reduces the effective radius to as low as 0.29 μm. Inversion of the reduced data set of $3\beta + 2\alpha$ does not significantly change the result. Because of the uncertainty of the particle backscatter coefficient at 1064, the mean value of volume concentration varies between 52 and 74 μm^3 cm^{-3}. In contrast, the complex refractive index is not affected by this error source.

With respect to the upper height layer we find a significantly lower effective radius of $0.19-0.24$ μm. Particle volume and surface-area concentration are lower by 50% and 20%, respectively. The complex refractive index remains rather unchanged. As in the case of the lower height range, we do not find significant differences for the retrieved parameters

Table 4. Optical Data for Two Measurement Cases Taken from INDOEX

Wavelength (nm)	Height Range			
	600–1000 m		1325–1650 m	
	α, km^{-1}	β, km^{-1} sr^{-1}	α, km^{-1}	β, km^{-1} sr^{-1}
355	0.394	0.00592	0.233	0.00332
400		0.00503		0.00292
532	0.274	0.00339	0.133	0.00192
710		0.0028		0.00169
800		0.0026		0.0016
1064		0.00214 [0.00145]		0.000869 [0.00144]

Table 5. Particle Parameters for a 600–1000-m Layer Retrieved from 6β + 2α and 3β + 2α Data Sets by Use of Volume Kernels[a]

Retrieved Parameters	6β + 2α	3β + 2α
r_{eff} (μm)	0.34 ± 0.13 [0.29 ± 0.12]	0.32 ± 0.12 [0.26 ± 0.1]
N_t (cm^{-3})	2500 ± 1700 [2800 ± 1900]	2000 ± 1400 [2100 ± 1400]
S_t (μm^2 cm^{-3})	680 ± 270 [680 ± 270]	670 ± 270 [610 ± 240]
V_t (μm^3 cm^{-3})	74 ± 30 [65 ± 30]	67 ± 30 [52 ± 20]
m_R	1.4 ± 0.05 [1.4 ± 0.05]	1.4 ± 0.05 [1.4 ± 0.05]
m_I	0.007 ± 0.0035 [0.006 ± 0.003]	0.006 ± 0.003 [0.006 ± 0.003]

[a]Values in brackets are obtained from the data set with backscatter at 1064 nm changed for $\beta_{1064} = 0.00145$ km^{-1} sr^{-1}.

from the reduced data set 3β + 2α. Some of the variability of the parameters between the two height layers might be attributed to the influence of the clouds in the lower height range.

This result can be compared with the findings presented in Ref. 3. In that analysis mainly the lower value of β_{1064} was considered. An effective radius of approximately 0.22 μm was found for both height ranges. Volume concentration varied around 44 ± 3.4 μm^3 cm^{-3}, and surface-area concentration was as high as 610 ± 50 μm^2 cm^{-3}. These numbers agree reasonably well with the results based on the use of the lower value of β_{1064} presented here. Acceptable agreement is also given for the complex refractive index. The real part of 1.35–1.39 reported in Ref. 3 is slightly lower than the values reported here. The imaginary part varies between 0.002i and 0.006i.

The value for effective radius for the measurement presented here is at the upper end of effective radii found for anthropogenic pollution from six-wavelength lidar observations in this area.[3,36] As mentioned before, broken clouds were found around 1000-m height. Next to the presence of cloud droplets and large particles caused by hygroscopic growths it is also reasonable to assume the presence of large marine particles injected from the marine boundary layer.

The assumption that water and/or sea salt contributed is supported by the value of the complex refractive index. The real part of 1.4 ± 0.05 indicates a mixture of anthropogenic pollution with water and sea-salt particles. The imaginary part of approximately 0.007 points to moderately absorbing particles. The contribution by nonabsorbing marine particles and water droplets could have led to these low values of the imaginary part. We emphasize that the six-wavelength lidar observations during the INDOEX showed that particles advected from South-east Asia to the Maldives were rather low absorbing in themselves,[3,31] resembling the absorption characteristics of aged European anthropogenic pollution observed with the six-wavelength lidar during the ACE 2.[37–39] ACE-2 was carried out in the North Atlantic/Portugal in June/July 1997.[40]

Figure 16(a) shows the retrieved size distribution for the lower height. It shows that the observed particles correspond to type I aerosol. The size distributions obtained from the 6β + 2α and 3β + 2α data sets are similar. Quite obviously there is a strong anthropogenic mode below 0.4 μm in the particle radius and two modes at larger particle sizes. The one between 1 and 10 μm clearly represents the coarse mode. One has to keep in mind that the uncertainty of β_{1064} has a significant influence on the presence of this coarse mode. In that respect the two clearly separable particle modes above approximately 0.4 mm have to be considered with some caution.

For comparison Fig. 16(b) shows the particle size distribution for the upper height layer. Obviously the coarse mode is not as pronounced as in Fig. 16(a). Again the influence of β_{1064} on the appearance of the particle size distribution is rather strong. It should be noted that the estimation of cloud droplet radii might also be performed with a Raman signal from water in a liquid state.[41] The comparison of these two methods is the plan for our future research.

5. Conclusion

We have presented a study on the retrieval of large particles in bimodal aerosol size distributions from multiwavelength lidar observations. The applied technique is Tikhonov's inversion with regularization. The studies focused mainly on the inversion of a combined data set of particle backscatter coefficients at 355, 532, and 1064 nm and extinction coef-

Table 6. Particle Parameters for a 1325–1650-m Layer Retrieved from 6β + 2α and 3β + 2α Data Sets by Use of Volume Kernels[a]

Retrieved Parameters	6β + 2α	3β + 2α
r_{eff} (μm)	0.19 ± 0.08 [0.24 ± 0.1]	0.2 ± 0.08 [0.26 ± 0.1]
N_t (cm^{-3})	3900 ± 2700 [4800 ± 3300]	2700 ± 1900 [2200 ± 1500]
S_t (μm^2 cm^{-3})	560 ± 220 [480 ± 190]	490 ± 190 [450 ± 180]
V_t (μm^3 cm^{-3})	34 ± 15 [38 ± 15]	31 ± 14 [39 ± 17]
m_R	1.42 ± 0.05 [1.43 ± 0.05]	1.4 ± 0.05 [1.43 ± 0.05]
m_I	0.007 ± 0.0035 [0.07 ± 0.0035]	0.005 ± 0.0025 [0.007 ± 0.0035]

[a]Values in brackets are obtained from data set with backscatter at 1064 nm changed for $\beta_{1064} = 0.00144$ km^{-1} sr^{-1}.
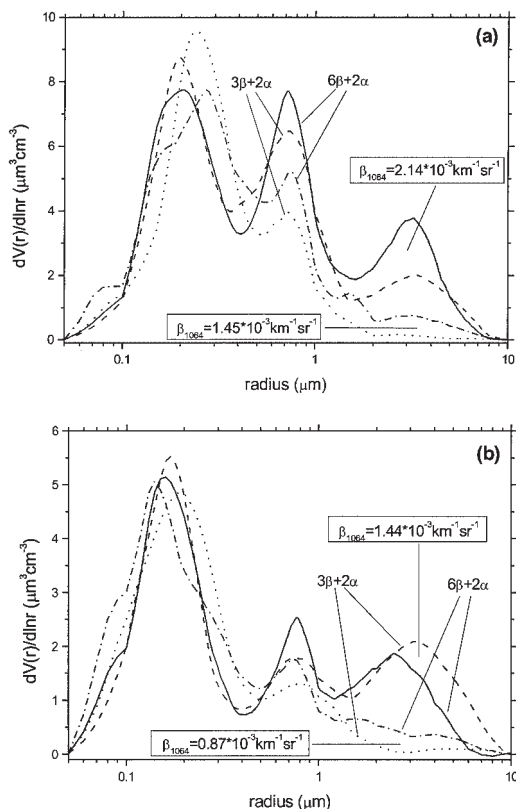
Fig. 16. Volume size distribution at (a) 600–1000-m and (b) 1325–1650-m layers retrieved from $6\beta + 2\alpha$ (solid, dash–dot) and $3\beta + 2\alpha$ (dash, dot) data sets by use of volume density kernels. The results were obtained for high (solid, dash) and low (dash–dot, dot) values of β_{1064}.

ficients at 355 and 532 nm. This data set is the minimum information needed for reliable retrieval of microphysical particle properties, i.e., effective radius, number, surface area, volume concentration, and complex refractive index. In principle such a data set can be provided by a multitude of aerosol lidar systems that operate on the basis of one Nd: YAG laser.

The inversion code had been modified from the previous version.[11] The use of data banks for Mie efficiencies and matrix elements used in the inversion allowed us to speed up the computation and to take into consideration particles with radii up to 20 μm. Compared with the previous code,[11] the accuracy of the inversion results was further optimized by a modification of the discrepancy principle that is used as the regularization element in the inversion. One of the advantages of this regularization approach is that knowledge of the measurement errors is not required. Depending on which microphysical parameter is retrieved a different set of kernel functions, i.e., number, surface area, volume, and fourth-order kernel functions, might provide somewhat better results. In that sense the stability and accuracy of the inversion is even further stabilized.

Studies dealt with the accuracy of the retrieved particle parameters and the ability of detecting the bimodal character of the size distributions. The bimodal structure was recognized by the inversion code in each case considered. Often there was a shift of the large mode toward larger particle sizes compared with the initially given mode. This shift also depends on the contribution of the coarse mode to the optical signal. In the worst case, the effective radius, number, surface area, and volume concentration were retrieved with an accuracy of 40%, 70%, 40%, and 45%, respectively. The real part of the complex refractive index could be retrieved to an accuracy of ±0.05. The accuracy of the imaginary part was always better than 50%.

The above numbers refer to size-independent complex refractive indices. Detailed studies were also done for cases in which each of the two modes had a different refractive index. These situations are particularly important as they describe external mixtures of aerosols. Under these conditions the effective radius, number, surface area, and volume concentration were retrieved with an average accuracy of 55%, 70%, 40%, and 50%, respectively.

For size distributions with an effective radius exceeding 2 μm, retrieval of the complex refractive index becomes difficult, because the kernel functions at big radii are not sensitive to variations in the real part. As a result, the retrieved real part is usually overestimated, whereas the effective radius and concentration are underestimated. This effect limits the retrieval of parameters of large particles. The situation could be somewhat improved if the particle refractive index were known, as, for example, in the case of aerosols with a large water content. From numerous simulations we conclude that the retrieval is still credible, if the ratio $|\beta_{532} - \beta_{1064}|/\beta_{532}$ is larger than the measurement error, which is approximately 10% in our case.

In the evaluation of the achieved accuracy of parameter retrieval presented in this paper we should keep in mind that only five years ago, before the implementation of new inversion techniques within the frame of development of Mie–Raman lidars at ITR, we could estimate only the order of magnitude of, e.g., the effective radius from tropospheric lidar observations. In that respect an accuracy of ~50% presents significant progress, which becomes even more valuable as this number holds not only for the simple case of monomodal particle size distributions,[9,11] but also for the more difficult case of bimodal size distributions. It allows estimating particle parameters presented in this study with an uncertainty lower than their respective natural variations described in Ref. 21, which is important in climate modeling. It should be noted that in existing models the tropospheric aerosol parameters are usually considered as height-independent quantities, which does not allow realistic simulations of, e.g., the aerosol indirect effect. The possibility to use the vertical distribution of aerosol parameters obtained from lidar measurements even with existing accuracy would be a significant improvement of such modeling. In that respect special interest lies in the continuation of

existing lidar networks such as EARLINET or the setup of new lidar networks in other regions of the world, or the development of airborne multiwavelength lidar, which would allow production of the global information of aerosol parameters.

Most of the studies presented here dealt with measurement errors of the order of 10%, which is the maximum accuracy that can be expected from Raman–Mie lidar systems. It should also be observed that atmospheric variability in that respect plays a key role under experimental conditions. Because the inversion code was extended toward dealing with large particles, e.g., large particles stemming from hygroscopic growth, we chose a measurement example of anthropogenic pollution between a broken cloud deck. The measurement was carried out during the INDOEX with the ITR six-wavelength aerosol lidar. In the lower height range of the pollution layer considered here we observed a strong coarse mode in the derived particle size distributions. This coarse mode might be the result of a large marine particle injected from the surface and/or hygroscopic growth of some of the particles as the result of high relative humidity. In the height range above the cloud deck we found smaller particles. Volume and surface-area concentration also were significantly lower. The real part of the complex refractive index of 1.4 was rather low in both height ranges. The imaginary part showed moderate absorption. These numbers also indicate the presence of large nonabsorbing marine particles and/or cloud droplets.

References

1. J. T. Houghton, Y. Ding, D. J. Griggs, M. Nouger, P. J. van der Linden, and D. Xiaosu, eds., *Third Assessment Report of Working Group I of the Intergovernmental Panel on Climate Change* (Cambridge University, Cambridge, England, 2001).

2. Y. J. Kaufman, D. Tanré, and O. Boucher, "A satellite view of aerosols in the climate system," Nature **419,** 215–223 (2002).

3. D. Müller, K. Franke, A. Ansmann, D. Althausen, and F. Wagner, "Indo–Asian pollution during INDOEX: Microphysical particle properties and single-scattering albedo inferred from multiwavelength lidar observations," J. Geophys. Res. **108**(D19), 4600, doi: 10.1029/2003JD003538, 2003.

4. D. Müller, A. Ansmann, F. Wagner, and D. Althausen, "European pollution outbreaks during ACE 2: microphysical particle properties and single-scattering albedo inferred from multiwavelength lidar observations," J. Geophys. Res. **107**(D15), 4248, doi: 10.1029/2001JD001110 (2002).

5. J. Heintzenberg, H. Müller, H. Quenzel, and E. Thomalla, "Information content of optical data with respect to aerosol properties: numerical studies with a randomized minimization-search-technique inversion algorithm," Appl. Opt. **20,** 1308–1315 (1981).

6. P. Qing, H. Nakane, Y. Sasano, and S. Kitamura, "Numerical simulation of the retrieval of aerosol size distribution from multiwavelength laser radar measurements," Appl. Opt. **28,** 5259–5265 (1989).

7. V. E. Zuev and I. E. Naats, eds., *Inverse Problems of Lidar Sensing of the Atmosphere* (Springer-Verlag, Berlin, 1983).

8. D. Müller, U. Wandinger, and A. Ansmann, "Microphysical particle parameters from extinction and backscatter lidar data by inversion with regularization: theory," Appl. Opt. **38,** 2346–2357 (1999).

9. D. Müller, U. Wandinger, and A. Ansmann, "Microphysical particle parameters from extinction and backscatter lidar data by inversion with regularization: simulation," Appl. Opt. **38,** 2358–2368 (1999).

10. D. Müller, F. Wagner, U. Wandinger, A. Ansmann, M. Wendisch, D. Althausen, and W. von Hoyningen-Huene, "Microphysical particle parameters from extinction and backscatter lidar data by inversion with regularization: experiment," Appl. Opt. **39,** 1879–1892 (2000).

11. I. Veselovskii, A. Kolgotin, V. Griaznov, D. Müller, U. Wandinger, and D. N. Whiteman, "Inversion with regularization for the retrieval of tropospheric aerosol parameters from multiwavelength lidar sounding," Appl. Opt. **41,** 3685–3699 (2002).

12. C. Böckmann, "Hybrid regularization method for ill-posed inversion of multiwavelength lidar data in the retrieval of aerosol size distributions," Appl. Opt. **40,** 1329–1342 (2001).

13. D. Althausen, D. Müller, A. Ansmann, U. Wandinger, H. Hube, E. Clauder, and S. Zörner, "Scanning six-wavelength eleven-channel aerosol lidar," J. Atmos. Ocean. Technol. **17,** 1469–1482 (2000).

14. D. Müller, U. Wandinger, D. Althausen, and M. Fiebig, "Comprehensive particle characterization from three-wavelength Raman lidar observations: case study," Appl. Opt. **40,** 4863–4869 (2001).

15. T. Murayama, N. Sugimoto, I. Uno, K. Kinoshita, K. Aoki, N. Hagiwara, Z. Liu, I. Matsui, T. Sakai, T. Shibata, K. Arao, B.-J. Shon, J.-G. Won, S.-C. Yoon, T. Li, J. Zhou, H. Hu, M. Abo, K. Iokibe, R. Koga, and Y. Iwasaka, "Ground-based network observations of Asian dust events of April 1998 in east Asia," J. Geophys. Res. **106,** 18345–18359 (2001).

16. J. Bösenberg, A. Ansmann, J. M. Baldasano, D. Balis, C. Böckmann, B. Calpini, A. Chaikovsky, P. Flamant, A. Hågård, V. Mitev, A. Papayannis, J. Pelon, D. Resendes, J. Schneider, N. Spinelli, T. Trickl, G. Vaughan, G. Visconti, and M. Wiegner, "EARLINET: a European Aerosol Research Lidar Network," in *Advances in Laser Remote Sensing*, A. Dabas, C. Loth, and J. Pelon, eds. (Ecole Polytechnique, Palaiseau, France, 2001), pp. 163–167.

17. J. Bösenberg, M. Alpers, D. Althausen, A. Ansmann, C. Böckmann, R. Eixmann, A. Franke, V. Freudenthaler, H. Giehl, H. Jäger, S. Kreipl, H. Linné, V. Matthias, I. Mattis, D. Müller, J. Sarközi, L. Schneidenbach, J. Schneider, T. Trickl, E. Vorobieva, U. Wandinger, and M. Wiegner, "The German Aerosol Lidar Network: methodology, data, analysis," MPI Report 317 (Max Planck Institute for Meteorology, Hamburg, Germany, 2001).

18. A. N. Tikhonov and V. Y. Arsenin, eds., *Solution of Ill-Posed Problems* (Wiley, New York, 1977).

19. S. Twomey, ed., *Introduction to the Mathematics of Inversion in Remote Sensing and Direct Measurements* (Elsevier, New York, 1977).

20. H. Horvath, R. L. Gunter, and S. W. Wilkison, "Determination of the coarse mode of the atmospheric aerosol using data from a forward-scattering spectrometer probe," Aerosol Sci. Technol. **12,** 964–980 (1990).

21. O. Dubovik, B. Holben, T. F. Eck, A. Smirnov, Y. J. Kaufman, M. D. King, D. Tanré, and I. Slutsker, "Variability of absorption and optical properties of key aerosol types observed in worldwide locations," J. Atmos. Sci. **59,** 590–608 (2002).

22. M. Hess, P. Koepke, and I. Schult, "Optical properties of aerosols and clouds: the software package OPAC," Bull. Am. Meteorol. Soc. **79,** 831–844 (1998).

23. Special issue on Tropospheric Aerosol Radiative Forcing Observational Experiment, J. Geophys. Res. **104,** D2 (1999).

24. Special issue on Tropospheric Aerosol Radiative Forcing Observational Experiment, J. Geophys. Res. **105,** D8 (2000).

25. Special issue on Aerosol Characterization Experiment 2, Tellus Ser. B **52,** No. 2 (2000).

26. Special issue on Indian Ocean Experiment, J. Geophys. Res. **107,** D19 (2002).

27. Special issue on Characterization of Asian Aerosols and Their Radiative Impacts on Climate, Part 1, J. Geophys. Res. **108,** No. 23 (2003).

28. Special issue on Lindenberg Aerosol Characterization Experiment, J. Geophys. Res. **107,** D21 (2002).

29. D. P. Donovan and A. I. Carswell, "Principal component analysis applied to multiwavelength lidar aerosol backscatter and extinction measurements," Appl. Opt. **36,** 9406–9424 (1997).

30. V. Ramanathan, P. J. Crutzen, J. Lelieveld, A. P. Mitra, D. J. Althausen, J. Anderson, M. O. Andreae, W. Cantrell, G. R. Cass, C. E. Chung, A. D. Clarke, J. A. Coakley, W. D. Collins, W. C. Conant, F. Dulac, J. Heintzenberg, A. J. Heymsfield, B. Holben, S. Howell, J. Hudson, A. Jayaraman, J. T. Kiehl, T. N. Krishnamurti, D. Lubin, G. McFarquhar, T. Novakov, J. A. Ogren, I. A. Podgorny, K. Prather, K. Priestley, J. M. Prospero, P. K. Quinn, K. Rajeev, P. Rasch, S. Rupert, R. Sadourny, S. K. Satheesh, G. E. Shaw, P. Sheridan, and F. P. J. Valero, "The Indian Ocean Experiment: an integrated analysis of the climate forcing and effects of the great Indo-Asian haze," J. Geophys. Res. **106,** 28371–28398 (2001).

31. K. Franke, A. Ansmann, D. Müller, A. Althausen, C. Venkataraman, M. Shekar Reddy, F. Wagner, and R. Scheele, "Optical properties of the Indo-Asian haze layer over the tropical Indian Ocean," J. Geophys. Res. **108** (D2), 4059, doi 10.1029/2002JD002473 (2003).

32. A. Ansmann, M. Riebesell, and C. Weitkamp, "Measurement of atmospheric aerosol extinction profiles with a Raman lidar," Opt. Lett. **15,** 746–748 (1990).

33. A. Ansmann, M. Riebesell, U. Wandinger, C. Weitkamp, E. Voss, W. Lahmann, and W. Michaelis, "Combined Raman elastic-backscatter lidar for vertical profiling of moisture, aerosol extinction, backscatter, and lidar ratio," Appl. Phys. B **55,** 18–28 (1992).

34. D. N. Whiteman, S. H. Melfi, and R. A. Ferrare, "Raman lidar system for measurement of water vapor and aerosols in the Earth's atmosphere," Appl. Opt. **31,** 3068–3082 (1992).

35. Y. Sasano, E. V. Browell, and S. Ismail, "Error caused by using a constant extinction/backscatter ratio in the lidar solution," Appl. Opt. **24,** 3929–3932 (1985).

36. D. Müller, K. Franke, F. Wagner, D. Althausen, A. Ansmann, and J. Heintzenberg, "Vertical profiling of optical and physical particle properties over the tropical Indian Ocean with six-wavelength lidar, 2, Case studies," J. Geophys. Res. **106,** 28577–28595 (2001).

37. A. Ansmann, F. Wagner, D. Althausen, D. Müller, A. Herber, and U. Wandinger, "European pollution outbreaks during ACE~2: Lofted aerosol plumes observed with Raman lidar at the Portuguese coast," J. Geophys. Res. **106,** 20725–20733 (2001).

38. A. Ansmann, F. Wagner, D. Müller, D. Althausen, A. Herber, W. von Hoyningen-Huene, and U. Wandinger, "European pollution outbreaks during ACE~2: Optical particle properties inferred from multiwavelength lidar and star/Sun photometry," J. Geophys. Res. **107** (D15), 4259, doi: 10.1029/2001JD001109 (2002).

39. D. Müller, A. Ansmann, F. Wagner, and D. Althausen, "European pollution outbreaks during ACE 2: Microphysical particle properties and single-scattering albedo inferred from multiwavelength lidar observations," J. Geophys. Res. **107** (D15), 4248, doi 10.1029/2001JD001110 (2002).

40. P. B. Russell and J. Heintzenberg, "An overview of the ACE~2 clear sky column closure experiment (CLEARCOLUMN)," Tellus Ser. B **52,** 463–483 (2000).

41. D. N. Whiteman and S. H. Melfi, "Cloud liquid water, mean droplet radius and number density measurements using a Raman lidar," J. Geophys. Res. **104**(D24), 31411–31419 (1999).